Chinese Chemical Letters 36 (2025) 110012

Contents lists available at ScienceDirect

Chinese Chemical Letters

journal homepage: www.elsevier.com/locate/cclet

Glucose-activated nanozyme hydrogels for microenvironment modulation *via* cascade reaction in diabetic wound

Yue Sun[1], Yingnan Zhu[1], Jiahang Si, Ruikang Zhang, Yalan Ji, Jinjie Fan, Yuze Dong*

School of Pharmaceutical Sciences, Institute of Drug Discovery and Development, Center for Drug Safety Evaluation and Research, Zhengzhou University, Zhengzhou 450001, China

ARTICLE INFO

Article history:
Received 6 March 2024
Revised 10 May 2024
Accepted 14 May 2024
Available online 15 May 2024

Keywords:
Metal-organic frameworks
Hybrid nanozyme
Glucose cascade reaction
Hydrogel
Diabetic wound healing

ABSTRACT

Wound healing in diabetic patients presents significant challenges due to heightened risks of bacterial infection, elevated glucose levels, and insufficient angiogenesis. Nanozymes are widely employed for wound healing, but most current nanozyme systems exhibit only moderate activity limited by incompatible reaction microenvironments including pH and hydrogen peroxide (H_2O_2) concentration. Herein, a glucose-activated nanozyme hydrogel was developed using bovine serum albumin (BSA)-modified gold nanoparticles (Au NPs) attached to a two-dimensional (2D) metal-organic framework (MOF) (Cu-TCPP(Fe)@Au@BSA) by an *in situ* growth method. The Au NPs function as a glucose oxidase (GOx)-like enzyme, converting glucose to gluconic acid and H_2O_2, triggering the peroxidase (POD)-like activity of Cu-TCPP(Fe) to produce hydroxyl radicals (•OH), effectively eliminating bacteria. Additionally, the modification of BSA reduces the Au NP size, enhancing enzyme activity. Both *in vitro* and *in vivo* tests demonstrate that this nanozyme hydrogel can be activated by the microenvironment to lower blood glucose, eliminate bacterial infections, and promote epithelial formation and collagen deposition, thus accelerating diabetic wound healing effectively. The multifunctional nanozyme hydrogel dressing developed in this study presents a promising therapeutic approach to enhance diabetic wound healing.

Diabetic ulcers present a significant challenge to healing due to various pathological features, including high glucose level, wound infection, insufficient angiogenesis and excessive reactive oxygen species (ROS) [1-3]. In severe cases, these ulcers may lead to the risk of amputation, posing substantial threats to patients' physical and mental health [4,5]. Consequently, the promotion of rapid and complete healing for diabetic ulcers remains a major obstacle [6,7]. Traditional wound dressings, although frequently utilized in treating diabetic wounds, often come with limited anti-infective properties and tend to adhere to the wound, hindering the healing process [8]. The emergence of wet healing theory introduced several wet wound dressings to address these challenges. Hydrogel dressings, with their high water content, excellent mechanical properties, porous and biocompatible nature, have gained great attention in wound healing [9,10]. To enhance the healing process, researchers have developed various hydrogel wound dressings with specialized functions. However, these hydrogels have typically been confined to a single function limiting their potential effectiveness [11,12]. Accordingly, the development of multifunctional hydrogels becomes crucial in expediting and enhancing diabetic wound healing, such as multiple injectable hydrogel [13], versatile immunomodulatory hydrogel [14] and so on [15-17]. Nanozymes have gained researchers' attention due to their low cost, high stability, and catalytic activity. Specifically, nanozymes have demonstrated multi-enzyme-like activity, holding promise to address issues in the diabetic microenvironment [18,19]. Metal-organic frameworks (MOFs) serve as a promising platform for emulating natural enzyme properties owing to their unique physicochemical characteristics, including high porosity and surface functionalization [20-22]. They have displayed potent peroxidase (POD)-like activity when copper or iron are used as metal nodes or when a porphyrin-iron structure (mimicking heme) is employed as a ligand. This structure is capable of eradicating bacteria by catalyzing the production of highly oxidative •OH from H_2O_2, thereby instigating chemodynamic therapy (CDT) [23,24]. Particularly, two-dimensional (2D) MOFs have high potential for biomedical applications due to their large surface area and active site exposure [25,26]. Additionally, nanozyme hydrogel can reinforce the delivery efficiency and provide a moist microenvironment, promoting wound healing [27,28].

* Corresponding author.
E-mail address: dongyuze@zzu.edu.cn (Y. Dong).
[1] These authors contributed equally to this work.

https://doi.org/10.1016/j.cclet.2024.110012
1001-8417/

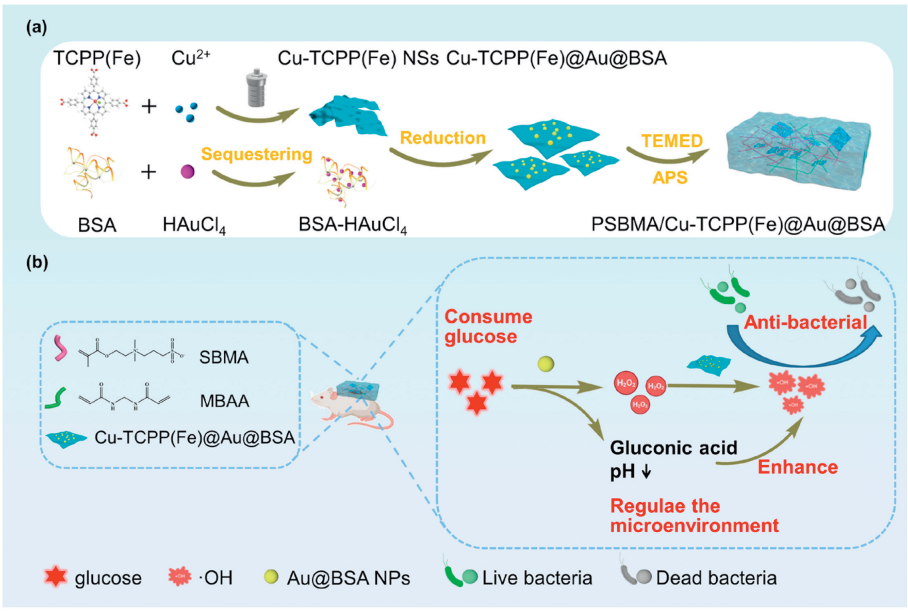

Scheme 1. (a) The preparation process of Cu-TCPP(Fe)@Au@BSA NSs and hydrogels. (b) Schematic illustration of PSBMA/Cu-TCPP(Fe)@Au@BSA hydrogels for promoting infected diabetic wound healing.

However, the MOF-based nanozymes used for wound healing usually exhibit activity in acidic solutions, posing a challenge in physiologically conditions and chronic wound which are typically weakly alkaline. Moreover, the physiological H_2O_2 concentration is insufficient for effective therapy, restricting their application in chemotherapy for anti-infection or anti-tumor. Therefore, the development of nanozymes with diverse enzyme activities is of paramount significance for modulating the complex microenvironment of diabetic wound.

Gold nanoparticles (Au NPs), served as glucose oxidase (GOx)-like enzyme, promote glucose consumption, pH reduction, and initiate H_2O_2 production [29,30]. This can regulate the wound microenvironment while overcome constrains posted by physiological pH and H_2O_2. However, Au NPs lack consistently small particle sizes and exhibit instability due to unmodifiable surfaces. It has been discovered that incorporating protein protectors enables Au NPs to display both GOx-like performance at the same pH level and improve their stability. In addition, the synergistic effects between Au NPs and carriers can further enhance enzyme-like performance [31]. Bovine serum albumin (BSA) stands out as a biomolecule because of easy accessibility, good biocompatibility and strong adaptability [32,33]. Consequently, the sulfhydryl group of BSA can modify Au NPs to obtain nanoparticles with enhanced activity and stability [34-36].

Herein, we constructed a multi-enzyme Cu-TCPP(Fe)@Au@BSA hydrogel for diabetic wounds healing (Scheme 1). Briefly, the BSA-modified Au NPs were integrated onto the 2D MOFs *via in situ* reduction and then loaded into the hydrogel. BSA decoration and the chemical composition of Cu-TCPP(Fe) led to a decrease in the particle size of Au NPs, which in turn enhanced the GOx-like activity. Au NPs metabolized glucose to create gluconic acid and H_2O_2, which could then be converted into $^{\bullet}OH$ through a cascade reaction activated by the iron porphyrin ligand in the resulting acidic conditions [37,38]. Subsequently, the nanozyme system was physically integrated into zwitterionic hydrogels, boosting biocompatibility and accelerating the healing process. It not only reduces glucose levels, but also efficiently catalyzes the production of $^{\bullet}OH$ at elevated concentrations of endogenous H_2O_2 in wound sites for CDT, and prompts tissue regeneration and restoration through epithelialization and collagen deposition. This study spotlights the promising potential of Cu-TCPP(Fe)@Au@BSA hydrogel as a significant promotion on wound healing.

After the successful synthesis of ligand TCPP(Fe) (Figs. S1 and S2 in Supporting information), the 2D MOF Cu-TCPP(Fe) was synthesized *via* surfactant-assisted method. Transmission electron microscopy (TEM) image revealed its lamellar structure measuring about 500 nm in size (Fig. S3a in Supporting information). The morphology remained unchanged after the *in situ* reduction of BSA-modified Au NPs. The distribution of Au NPs on the surface of Cu-TCPP(Fe) was random (Figs. S3b and c in Supporting information). The high-resolution TEM further proved that the black dot in Fig. S3d (Supporting information) was AuNPs, which was firmly immobilized on the surface of 2D MOF with the help of $NaBH_4$. As shown in Figs. S4 and S5 (Supporting information), elemental scans and the ultraviolet–visible (UV–vis) absorption peak at 528 nm were utilized to confirm the presence of Au NPs. The aggregation of pure Au NPs and the change in peak position (blue line) confirmed that the presence of Cu-TCPP(Fe) enhanced the distribution of Au NPs due to the interaction of N groups of MOFs with Au elements [39]. Furthermore, the Au NPs in Cu-TCPP(Fe)@Au@BSA (with particles averaging 15.79 nm in size) were smaller compared to pure Au NPs, which can expose more active sites to enhance enzymatic activity (Fig. S6 in Supporting information). Scanning electron microscopy (SEM) elemental mapping of Cu-TCPP(Fe)@Au@BSA revealed the distribution of C, N, O, Fe, Cu, Au, and S elements. The consistent distribution of sulfur with Au elements suggested that BSA successfully modified Au NPs (Fig. S7 in Supporting information). X-ray photoelectron spectroscopy (XPS) results demonstrated consistent elemental compositions. Fig. S8 (Supporting information) presented the complete XPS spectra for both materials. In Fig. S9 (Supporting information), the peaks observed at 711.38 eV and 724.78 eV on the high-resolution XPS spectra of Fe 2p were assigned to Fe-N $2p_{3/2}$ and Fe-N $2p_{1/2}$ in the porphyrin-iron ligand, respectively [40], and the signals at 932.98, 934.98, 952.28 and 954.98 eV could be separately attributed to the Cu^+ $2p_{3/2}$, Cu^{2+} $2p_{3/2}$, Cu^+ $2p_{1/2}$, Cu^{2+} $2p_{1/2}$. Additionally, the high-resolution XPS spectra of O 1s indicated successful synthesis of Cu and TCPP(Fe) ligands (-COOH) resulting in the successful formation of MOF nanosheets [41]. The peaks at 84.4 and 87.9 eV corresponded to the characteristic peaks of Au $4f_{7/2}$ and Au $4f_{5/2}$

of Au, respectively [42]. This indicated that the Au was in a metallic state in MOF nanosheets, allowing them to imitate the GOx-catalyzed reaction. The change in zeta potential also confirmed the successful loading of Au NPs (Fig. S10 in Supporting information). X-ray diffraction (XRD) patterns in Fig. S11 (Supporting information) exhibited distinctive diffraction peaks for both materials. Two major peaks corresponded to the (001) and (002) crystal planes of Cu-TCPP(Fe) consistent with the previous results. Peaks at the 44.3° and 77.7° for Cu-TCPP(Fe)@Au@BSA were attributed to (200) and (311) crystal planes of Au, respectively, demonstrating the *in situ* synthesis of Au NPs [43]. Notably, Cu-TCPP(Fe) displayed comparable diffraction spectra before and after modification, suggesting that the crystal structure was not influenced by Au NPs. Additionally, the Cu-TCPP(Fe)@Au@BSA sample exhibited reduced peak intensity compared to those of Cu-TCPP(Fe) owing to the surface modification. The step-by-step synthesis process was analyzed using Fourier transform infrared spectroscopy (FTIR) (Fig. S12 in Supporting information). Characteristic absorption peaks at 1000 cm^{-1} belonged to the Fe-N. Vibration peaks between 1700 cm^{-1} and 1680 cm^{-1}, corresponding to (-COOH), exhibited strong intensity, but weakened in the spectra of Cu-TCPP(Fe), indicating coordination of (-COOH) with Cu [44]. The distinct characteristic peaks were slightly shifted due to the *in situ* formation of Au NPs.

The pure amphiphilic poly(sulfobetaine methacrylate) (PSBMA) hydrogel was crosslinked through thermal initiation to form a gel [45]. Nanocomposite hydrogels were then produced by physically incorporating nanoparticles into the precursor gel solution, followed by crosslinking, designated as PSBMA/Cu-TCPP(Fe)@Au@BSA (Fig. S13a in Supporting information). SEM analysis revealed a porous network structure for both hydrogels, with a pore size of approximately 25 μm. Notably, the internal structure of the hydrogels remained unchanged even after the introduction of nanoparticles (Fig. S13b in Supporting information). Furthermore, the rheological behavior was studied by a Rheometer. The time-sweep curves revealed that the dynamic storage modulus (G') of all the hydrogels consistently exceeded their loss modulus (G'') at a frequency of 1 Hz and a strain of 1%, indicating the successful formation of the hydrogel and its stable, solid-like behavior (Fig. S14 in Supporting information). Fig. S15 (Supporting information) illustrated the adhesive properties of the PSBMA hydrogel, displaying its secure attachment to flexed finger joints. Additionally, the hydrogel exhibited impressive mechanical properties, demonstrated by its ability to return to its original state after compression and stretching. The hydrogel's mechanical properties were also evaluated through compressive testing, achieving a compressive stress of 9.3 MPa, approximately 100 times greater than that of the poly(2-hydroxyethyl methacrylate) (PHEMA) hydrogel (Fig. S16 in Supporting information). Hydrogel with high water content and strong uptake characteristics contribute to a moist environment for wound and effectively absorb exudate and debris [46]. As depicted in Fig. S17 (Supporting information), the hydrogel had a water content exceeding 60%, surpassing the PHEMA hydrogel with around 40%. Besides, Fig. S18 (Supporting information) illustrated the real-time uptake behavior of the hydrogel in phosphate buffered saline (PBS) buffer, reaching 200% uptake after 9 h. Both hydrogels showed excellent uptake performance in 0.9% NaCl solution and PBS buffer, with the PSBMA/Cu-TCPP(Fe)@Au@BSA hydrogel reaching a peak uptake rate of 250% particularly noteworthy in 0.9% NaCl solution, which offered potential clinical advantages. The high uptake was attributed to the disruption of zwitterionic moieties' interactions by the ions in the salt solution [47]. Following the incorporation nanoparticles into the hydrogel, they were co-incubated with either H_2O_2 or glucose. Subsequently, a 3,3′,5,5′-tetramethylbenzidine (TMB) was introduced as a color developer to evaluate the POD-like activity. The experiment results demonstrated that the enzymatic hydrogel composites have the capability to catalyze the production of $^{\bullet}OH$ from H_2O_2 and can undergo cascade reactions (Fig. S19 in Supporting information). These findings suggest potential applications in treating diabetic wounds.

The cascade reaction was illustrated schematically in Fig. 1a. The Au NPs acted as a GOx-like enzyme, decomposing glucose into H_2O_2, while Cu-TCPP(Fe) were used as a POD-like enzyme to further decompose it to $^{\bullet}OH$. The TMB chromogenic method was employed to detect the $^{\bullet}OH$ producing ability of Cu-TCPP(Fe), Cu-TCPP(Fe)@Au and Cu-TCPP(Fe)@Au@BSA (Fig. 1b). The addition of the nanozymes produced an absorption peak at 652 nm, accompanied by a color change from colorless to blue, indicating their capability to catalyze H_2O_2. Additionally, the absorption peaks increased after loading with Au NPs, attributed to the hybridization of MOF with metal nanoparticles, imparting a synergistic catalytic effect and enhancing POD-like activity [48]. Moreover, the catalytic activity of Cu-TCPP(Fe)@Au@BSA was 2.21 and 1.77 times higher than that of Cu-TCPP(Fe) and Cu-TCPP(Fe)@Au, respectively. The alteration in absorbance at 652 nm of Cu-TCPP(Fe)@Au@BSA catalyzed H_2O_2 with varying concentrations was also monitored in real-time for the initial ten minutes. As illustrated in Fig. 1c, the concentration increased, and the absorbance continued to rise over time. To quantify the POD-like enzyme activity, the steady-state kinetics of its various catalytic substrates were investigated. The Michaelis-Menten constant (K_m) and the maximum initial velocity (V_{max}) were determined by modifying the concentrations of H_2O_2 and TMB using the Michaelis-Menten kinetics and Lineweaver-Burk equations. Figs. 1d and e demonstrated the variation in the reaction rate with H_2O_2 concentration or TMB concentration (Fig. S20 in Supporting information), revealing an increase in the reaction rate with substrate concentration. The inverse of the substrate concentration correlated linearly with the inverse of the initial rate. The K_m of H_2O_2 and TMB were calculated to be 0.74 and 0.34 mmol/L. They were 5 and 1.28 times lower than HRP, respectively, and lower than that of most previously developed natural enzymes, metal-organic frameworks, iron-based nanozymes, *etc.*, indicating the good affinity for different substrates (Fig. S21 in Supporting information). After centrifuging the supernatant, HRP and TMB were added to generate color, as shown in Fig. 1f. There was poor GOx-like activity in the presence of Cu-TCPP(Fe)@Au, but a 28% increased absorption peak at 652 nm with a darker color, potentially due to BSA modification and chemical dispersion of the nanosheets, leading to a reduced particle size of the Au NPs and an enhancement of catalytic activity. The H_2O_2 product resulting from the glucose decomposition by Cu-TCPP(Fe)@Au@BSA was detected through $KMnO_4$ colorimetry. The generation of the product was confirmed by the fading of $KMnO_4$ and the disappearance of the UV absorption peaks (Fig. 1g). Fig. 1h depicted an increase in absorption peaks with varying nanozyme concentration levels in the cascade reaction, indicating an accompanying increase in concentration. Moreover, the catalytic activity of Cu-TCPP(Fe)@Au@BSA nanosheets towards H_2O_2 and glucose was strongly influenced by pH, exhibiting superior catalytic performance in an acidic rather than a neutral setting (Fig. S22 in Supporting information). The pH of the mixture solution of Cu-TCPP(Fe)@Au@BSA and glucose decreased around 4.11 after the reaction for 24 h, referring to the produce of gluconic acid. Given the abundance of glucose of diabetic wounds, the devised nanozymes may utilize glucose and instigate a cascade reaction stimulating $^{\bullet}OH$ production, thereby conferring an effective therapeutic effect. Electron paramagnetic resonance (EPR) spectroscopy was utilized to identify free radicals. Fig. S23 (Supporting information) indicated that catalyzing H_2O_2 produced a distinct splitting peak with a characteristic signal of 1:2:2:1, attributed to the presence of $^{\bullet}OH$. Subsequently, incubation with glucose resulted in characteristic signal peaks of H_2O_2 and $^{\bullet}OH$ due to the cascade reaction.

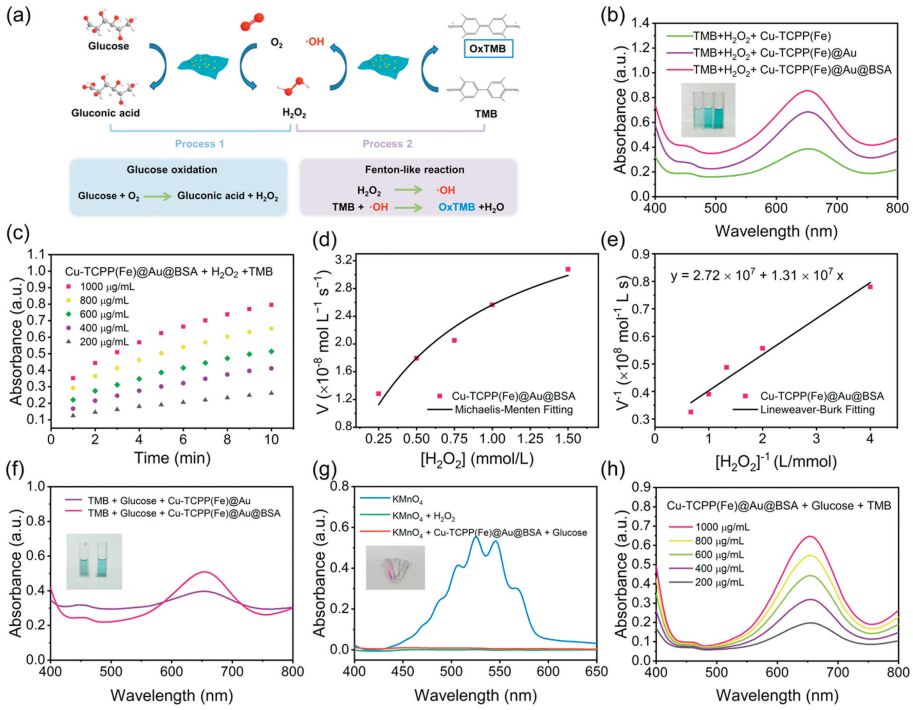

Fig. 1. Activity test of nanozymes. (a) Schematic diagram of the cascade reaction. (b) Comparison of POD-like activities of various nanozymes. (c) Time-dependent absorbance changes with the addition of different concentrations of Cu-TCPP(Fe)@Au@BSA. (d) Michaelis-Menten kinetics and (e) Lineweaver-Burk of Cu-TCPP(Fe)@Au@BSA for H_2O_2. (f) Comparison of GOx-like activities of various nanozymes. (g) Detection of product H_2O_2. (h) UV–vis absorption spectra of cascade reactions with different concentrations of Cu-TCPP(Fe)@Au@BSA.

Escherichia coli (*E. coli*) and *Staphylococcus aureus* (*S. aureus*) were utilized as model bacteria to assess the *in vitro* antibacterial efficacy of Cu-TCPP(Fe)@Au@BSA using the plate counting method [49]. The results indicated that concentrations of 100 μg/mL and 75 μg/mL achieved 99% antibacterial ratio against *E. coli* and *S. aureus*, respectively (Fig. S24 in Supporting information). Figs. 2a and b demonstrated that the Cu-TCPP(Fe)@Au group resulted in a notable antibacterial effect compared to the control group, with a bacterial survival rate less than 40% (100 μg/mL for *E. coli* and 75 μg/mL for *S. aureus*). This result was ascribed to the cascade reaction, where Au NPs could emulate the catalyzed production of H_2O_2 from glucose by GOx-like, contributing to local acidification and producing antibacterial ·OH. Based on the results, the Cu-TCPP(Fe)@Au@BSA group exhibited an almost 99% antimicrobial effect against both bacteria, potentially attributed to the existence of BSA within the group (100 μg/mL for *E. coli* and 75 μg/mL for *S. aureus*). In addition, consistent trends were observed in the results of fluorescent staining experiments of live and dead bacteria (Fig. S25 in Supporting information). These outcomes suggested that the created nanozymes were capable of eliminating a diverse assortment of bacteria and have efficacy against both Gram-positive and Gram-negative bacteria. To explore the antibacterial mechanism of nanozymes, the production of ROS was confirmed by co-incubating *E. coli* or *S. aureus* with DCFH-DA fluorescent probe. The fluorescence intensity was strengthened in proportion to the amount of ROS produced. Green fluorescence was observed in both the Cu-TCPP(Fe)@Au and Cu-TCPP(Fe)@Au@BSA groups when co-incubated with glucose and bacterial solution for 3 h, as illustrated in Fig. 2c. In contrast, the other groups showed almost no fluorescence detection. The level of ROS in the Cu-TCPP(Fe)@Au@BSA group was higher compared to the Cu-TCPP(Fe)@Au group, suggesting that the catalytic performance of the enzyme was influenced by BSA modification. The Au NPs modified with BSA exhibited enhanced GOx-like activity, triggering a cascade reaction leading to bacterial death *via* increased ROS production. These findings align with the *in vitro* antibacterial effect.

Bacterial colonization of wounds to form biofilms can impede wound healing. Fig. 2d demonstrated concentration dependence regarding the anti-biofilm activity. Most biofilms remained intact in the control groups, while biofilms in the Cu-TCPP(Fe)@Au@BSA group were severely disrupted. A concentration of 100 μg/mL was the most effective for a 70% reduction in biofilm, and increasing the concentration to 200 μg/mL resulted in an 85% reduction in biofilm. Live/dead fluorescence staining further validated the antibiofilm performance (Fig. 2e). When the concentration rised to 200 μg/mL, the majority of *S. aureus* in the biofilm were killed, with only a small number of bacteria stained green. This indicated that the Cu-TCPP(Fe)@Au@BSA at a concentration of 200 μg/mL can effectively facilitate the elimination of *S. aureus* bacterial biofilms, which was ascribe to the consumption of oxygen as well as the generation of ·OH by the catalytic effect of Cu-TCPP(Fe)@Au@BSA in the presence of glucose [50,51].

Hydrogels must adhere to high biocompatibility standards for their application as wound dressings. Cytocompatibility evaluation was performed using the CCK8 method and live-dead cell staining assay. After loaded with the particles, the cell activities of different concentrations of PSBMA/Cu-TCPP(Fe)@Au@BSA co-incubated with NIH-3T3 cells, HeLa cells, and RAW 264.7 cells for 3 days were shown in Figs. S26b-d (Supporting information). Cells demonstrated excellent cytocompatibility with materials at concentrations of 100 μg/mL and below after incubation, with cell activity remaining above 80% even at the higher concentration of 200 μg/mL. Fig. S26a (Supporting information) presented the cell growth status after 3 days of incubation following live-dead fluorescent staining, revealing a significant amount of green fluorescence indicative of live cells. Additionally, the blood compatibility of the hydrogels was evaluated using a hemolysis assay (Fig. S26e in Supporting information). The results showed that the hemolysis rate

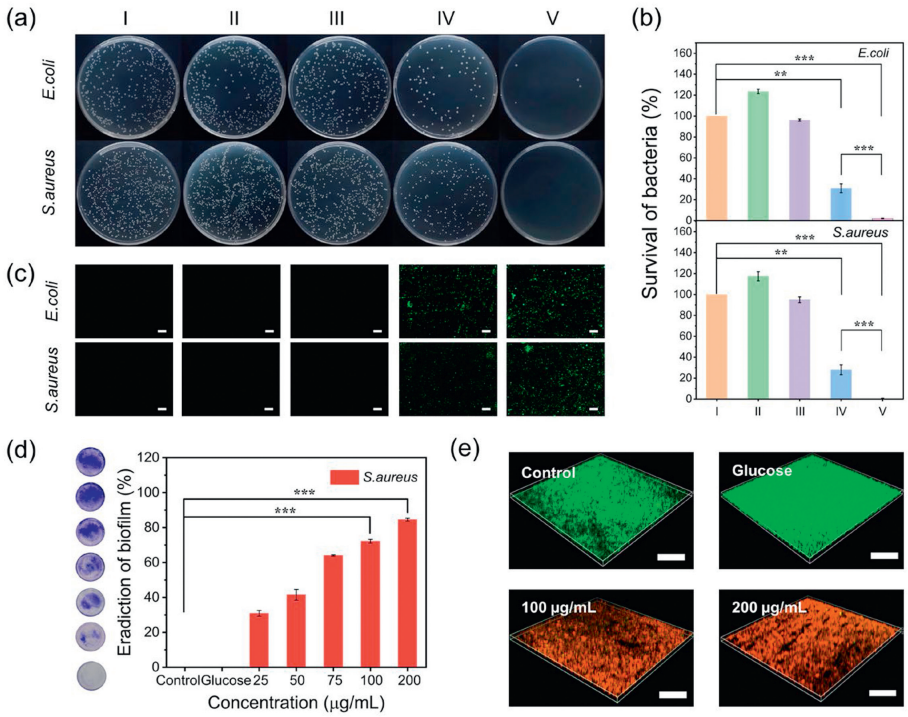

Fig. 2. *In vitro* antimicrobial activity. (a) Plate antimicrobial pictures and (b) corresponding survival rates of *E. coli* and *S. aureus* (I: PBS. II: glucose. III: Cu-TCPP(Fe) + glucose. IV: Cu-TCPP(Fe)@Au + glucose. V: Cu-TCPP(Fe)@Au@BSA + glucose). (c) Fluorescent images of intracellular ROS in *E. coli* and *S. aureus* induced by different samples detected with DCFH-DA probes (Scale bar: 100 μm). (d) Crystal violet staining images of treated *S. aureus* biofilms and corresponding eradication rate of biofilm. (e) CLSM image of treated *S. aureus* biofilms after staining with calcein/PI kit (Scale bar: 100 μm). Data are presented as mean ± SD ($n = 3$). $^{**}P < 0.01$, $^{***}P < 0.001$.

of PSBMA/Cu-TCPP(Fe)@Au@BSA at concentrations varying from 0 to 200 μg/mL was less than 5%.

The efficacy of the designed hydrogel dressing in promoting healing was validated through a diabetic wound model with *S. aureus* infection (Fig. 3a). All animal experiment procedures were approved by the Animal Care and Use Committee of Pharmacy College, Zhengzhou University and all procedures were complied with the Laboratory Animal Requirements of Environment and Housing Facilities. Photographs of the wounds were taken at various time points during treatment, and wound healing process was assessed by measuring the wound area. Fig. 3b showed the presence of pus in all wound sites 24 h after infection, confirming the success of the bacterial infection model. Starting from day 2, no excess exudate was observed in the hydrogel dressing group, indicating its efficacy in managing wound exudate. Zwitterionic hydrogel dressings exhibited superior exudate absorption and wound moisture maintenance compared to PHEMA hydrogel due to their high water content and rapid dissolution rate. After 12 days of treatment, the group treated with PSBMA/Cu-TCPP(Fe)@Au@BSA hydrogel displayed the best healing effect with a wound healing rate of 87.2%, along with less scarring, while other groups still remained distinguished wounds (Fig. 3c). This was attributed to the combined effects of the hydrogel and Cu-TCPP(Fe)@Au@BSA. To evaluate bacterial presence at the infected wound site following various treatments, skin wound tissue was collected on day 2 and day 12, and bacterial counts were obtained using the smear plate technique. Following 12 days of treatment, the PSBMA/Cu-TCPP(Fe)@Au@BSA hydrogel group eradicated 99.99% *S. aureus* from wound tissues. Additionally, the bacterial concentration in the two remaining control groups was significantly higher than that in the PSBMA/Cu-TCPP(Fe)@Au@BSA hydrogel group, which was 907 and 455 times higher, respectively (Fig. 3d). In addition, neither the test nor the control groups had a statistically discernible change in the body weight of mice during the treatment period (Fig. 3e). Hematoxylin and eosin (H&E) and Masson's trichrome staining were conducted on the wound sites on day 2 and day 12, respectively, to evaluate the therapeutic efficacy of the composite hydrogel on diabetic infected wounds. As shown in Figs. S27a and c (Supporting information), after 2 days of treatment, the skin epidermis was absent and there was a large infiltration of inflammatory cells in the tissue (black arrows and red dashed box), which persisted in all groups even after 12 days of treatment. However, the PSBMA/Cu-TCPP(Fe)@Au@BSA hydrogel treatment revealed the best histological outcomes, with decreased inflammatory cells and the emergence of thicker new epidermal structures compared to other groups (dashed and solid red lines). The Masson staining results from a 12-day treatment demonstrated a visible emergence of skin appendages, including sebaceous glands and hair follicles (yellow arrows). The control group has a large amount of inflammatory cell immersion. In contrast, the PSBMA/Cu-TCPP(Fe)@Au@BSA hydrogel group can be observed in a more aligned collagen fibers and denser collagen deposition (Figs. S27b and d in Supporting information). To evaluate the biosafety of the hydrogel *in vivo*, H&E staining of major organs was conducted after 12 days of treatment (Fig. S28 in Supporting information). Compared with the control group, all experimental groups exhibited no abnormal damage, demonstrating that the hydrogel wound dressing had a reliable safety profile without any apparent toxic side effects. This is consistent with the results of wound healing *in vivo*, indicating that the designed hydrogel composites facilitated the healing of diabetic wounds by promoting antimicrobial activity, accelerating epithelial formation, and depositing collagen, all while posing no biosafety risks.

In conclusion, we developed a glucose-activated nanozyme hydrogel based on Cu-TCPP(Fe)@Au@BSA nanozyme with dual enzyme activity as a wound dressing in diabetic bacterial infected wounds. The BSA decoration and the chemical composition of Cu-TCPP(Fe) led to a decreased particle size of Au NPs, which

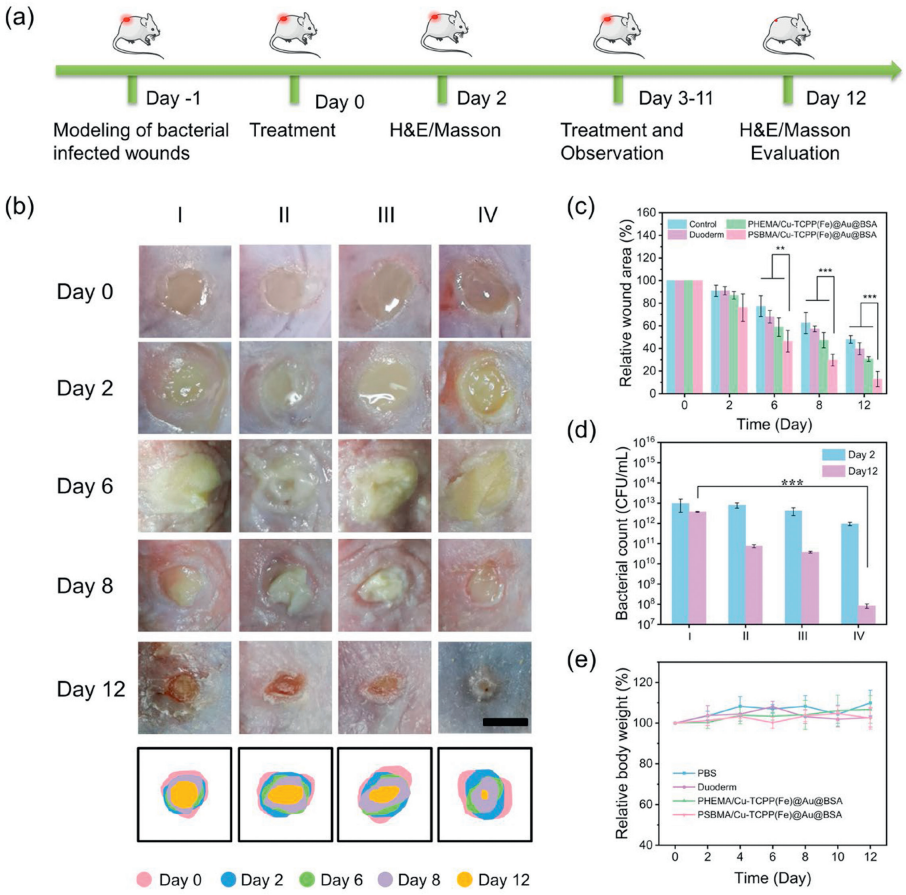

Fig. 3. *In vivo* assessment of diabetic wound healing. (a) Schematic diagram for diabetic infected wound construction and treatment process (I: PBS. II: Duoderm. III: PHEMA/Cu-TCPP(Fe)@Au@BSA. IV: PSBMA/Cu-TCPP(Fe)@Au@BSA). (b) Representative images of wounds from diverse groups at various time points (Scale bar: 5 mm). (c) Analysis of changes in relative wound area ($n = 5$). (d) Bacterial concentration at the wound site on days 2 and 12 ($n = 3$). (e) Analysis of changes in relative body weight ($n = 5$). Data are presented as mean ± SD. $^{**}P < 0.01$, $^{***}P < 0.001$.

enhanced the GOx-like activity. Thanks to the designed BSA-decorated Au NPs as well as the synergetic effects of Au NPs and 2D MOFs, the nanozyme exhibited high glucose-activated cascade activity, which can be spontaneously activated by the diabetic wound microenvironment. These nanozymes eliminated bacteria by oxidizing glucose to generate H_2O_2 through GOx-like activity and induced POD-like activity to release $^{\bullet}OH$. *In vitro* experiments presented a good antibacterial rate both for Gram-positive bacterial (99.61%) and Gram-negative bacterial (98%) infections. Additionally, the prepared hydrogel dressing exhibited remarkable biocompatibility and significant therapeutic efficacy with a good wound healing rate of 87.2%. *In vivo* animal experiments further demonstrated that Cu-TCPP(Fe)@Au@BSA hydrogel facilitated the healing of diabetic wounds by preventing wound infections, promoting epithelialization and collagen deposition. Therefore, the glucose-activated nanozyme hydrogels offer a novel approach for the clinical treatment of diabetic wounds.

Declaration of competing interest

The authors declare that they have no known competing financial interests or personal relationships that could have appeared to influence the work reported in this paper.

CRediT authorship contribution statement

Yue Sun: Writing – review & editing, Writing – original draft, Methodology, Investigation, Formal analysis, Conceptualization. **Yingnan Zhu:** Writing – review & editing, Writing – original draft, Investigation, Formal analysis, Conceptualization. **Jiahang Si:** Validation, Methodology, Investigation. **Ruikang Zhang:** Writing – review & editing, Methodology, Investigation. **Yalan Ji:** Investigation. **Jinjie Fan:** Methodology. **Yuze Dong:** Writing – review & editing, Supervision, Project administration, Funding acquisition, Conceptualization.

Acknowledgments

This work was supported by the National Natural Science Foundation of China Project (No. 22208321), the China Postdoctoral Science Foundation Project (No. 2022M720130), the Key Scientific Research Project of Henan Province High Education Institutions (No. 24A350018), and the Natural Science Foundation of Henan Province-Outstanding Youth Foundation (No. 232300421058).

Supplementary materials

Supplementary material associated with this article can be found, in the online version, at doi:10.1016/j.cclet.2024.110012.

References

[1] Z. Liang, J. Luo, S. Liu, et al., Chem. Eng. J. 475 (2023) 146092.
[2] L. Yang, D. Zhang, W. Li, et al., Nat. Commun. 14 (2023) 7658.
[3] F. Huang, X. Lu, Y. Yang, et al., Adv. Sci. 10 (2023) e22033088.
[4] K. McDermott, M. Fang, A.J.M. Boulton, E. Selvin, C.W. Hicks, Diabetes Care 46 (2023) 209–221.

[5] Y. Hu, Y. Wang, F. Yang, et al., Adv. Sci. 11 (2023) 2307746.
[6] X. Zhang, Z. Wang, H. Jiang, et al., Sci. Adv. 9 (2023) eadh1415.
[7] J. Chen, Z. Mu, D. Chen, et al., Chem. Eng. J. 469 (2023) 143985.
[8] F. Wang, Q. Sun, Y. Li, et al., Adv. Sci. 11 (2023) 2305078.
[9] Y. Chen, X. Wang, S. Tao, et al., Mil. Med. Res. 10 (2023) 37.
[10] Y.T. Xu, J.F. Hu, J.J. Hu, et al., Prog. Polym. Sci. 146 (2023) 101740.
[11] Y. Fang, S. Huang, X. Gong, et al., Acta Biomater. 158 (2023) 239–251.
[12] Y. Zhao, B. Yi, J. Hu, et al., Adv. Funct. Mater. 30 (2023) 1910748.
[13] X.L. Qi, E.Y. Cai, Y.J. Xiang, et al., Adv. Mater. 35 (2023) 2306632.
[14] X.L. Qi, Y.J. Xiang, E.Y. Cai, et al., Chem. Eng. J. 439 (2022) 135691.
[15] J.J. Wang, X.X. Ge, Y.J. Xiang, et al., Chin. Chem. Lett. 36 (2025) 109819.
[16] P. Yang, Z.P. Gu, F. Zhu, Y.W. Li, CCS Chem. 2 (2020) 128–138.
[17] H.J. Zhang, C.H. Huang, J.H. Zhang, et al., Giant 12 (2022) 100120.
[18] L.M. Shang, Y.X. Yu, Y.J. Jiang, et al., ACS Nano 17 (2023) 15962–15977.
[19] J. Sheng, Y. Wu, H. Ding, et al., Adv. Mater. 36 (2023) 2211210.
[20] Z.Y. Chen, S. Song, H.J. Zeng, et al., Chem. Eng. J. 471 (2023) 144649.
[21] Y. Tang, Y. Han, J. Zhao, et al., Nano-Micro Lett. 15 (2023) 112.
[22] M.K. Sarangi, L.D. Patel, G. Rath, et al., Chin. Chem. Lett. 35 (2024) 109381.
[23] X. Liu, Z. Yan, Y. Zhang, et al., ACS Nano 13 (2019) 5222–5230.
[24] S.W. Zhuang, H.J. Xiang, Y.X. Chen, et al., J. Nanobiotechnol. 20 (2022) 66.
[25] N. Wang, W. Liu, G. Chai, et al., Chem. Eng. J. 477 (2023) 147262.
[26] Y. Lin, L. Li, Z. Shi, et al., Small 20 (2024) 2309841.
[27] F. Zhang, Y. Kang, L.W. Feng, et al., Mater. Horiz. 10 (2023) 5474–5483.
[28] G.L. Le, Y.Q. Li, L. Cai, et al., Chem. Eng. J. 477 (2023) 146421.
[29] J. Chen, Q. Ma, M. Li, et al., Nat. Commun. 12 (2021) 3375.
[30] W. Luo, C. Zhu, S. Su, et al., ACS Nano 4 (2010) 7451–7458.
[31] H. Zhang, X. Liang, L. Han, F. Li, Small 14 (2018) 1803256.
[32] T. Zhao, B. Gong, S. Luo, et al., Acta. Biomater. 167 (2023) 574–582.
[33] V. Kalidasan, X.L. Liu, T.S. Herng, Y. Yang, J. Ding, Nano-Micro Lett. 8 (2016) 80–93.
[34] Y. Li, D. Zhang, Y. Yu, et al., ACS Nano 17 (2023) 16993–17003.
[35] Z. Liu, J. Zhang, H. Liu, et al., Adv. Mater. 35 (2023) 2208692.
[36] Y. Li, R.Z. Fu, Z.G. Duan, C.H. Zhu, D.D. Fan, Small 18 (2022) e2200165.
[37] C. Zhong, C. Hu, D. Ouyang, et al., Chem. Eng. J. 477 (2023) 146979.
[38] J. Chen, H. Gao, Z. Li, et al., Chin. Chem. Lett. 31 (2020) 1398–1401.
[39] W.C. Hu, M.R. Younis, Y. Zhou, C. Wang, X.H. Xia, Small (16) (2020) 2000553.
[40] H. Zhang, H. Wu, X. Qin, et al., Food Chem. 384 (2022) 132552.
[41] Y. Zhou, B. Zheng, L.M. Lang, G.X. Liu, X.H. Xia, ACS Appl. Nano Mater. 5 (2022) 18761–18769.
[42] X.M. Zeng, Y.H. Ruan, Q. Chen, S.Q. Yan, W. Huang, Chem. Eng. J. 452 (2023) 138422.
[43] H. Wang, J. Han, W. Lu, et al., J. Colloid Interface Sci. 440 (2015) 236–244.
[44] K. Li, C. Lin, M. Li, et al., ACS Nano 16 (2022) 2381–2398.
[45] Y. Fang, S. Huang, Q. Hu, et al., ACS Nano 17 (2023) 24883–24900.
[46] Y. Gong, P. Wang, R. Cao, et al., ACS Nano 17 (2023) 22355–22370.
[47] X. Li, C. Tang, D. Liu, et al., Adv. Mater. 33 (2021) 2102479.
[48] P. Wu, F. Gong, X. Feng, et al., J. Nanobiotechnol. 21 (2023) 185.
[49] Z.P. Li, Q.C. Feng, J.L. Shen, Chin. Chem. Lett. 35 (2024) 109602.
[50] L.Y. Zou, X. Li, Y. Huang, et al., Nano Today 50 (2023) 101828.
[51] J.Y. Zhang, M.D. Lv, X.Y. Wang, et al., Small 19 (2023) 2302587.